# Modeling Noise and Modulation Performance of Fiber Grating External Cavity Lasers

Malin Premaratne, *Student Member, IEEE,* Arthur J. Lowery, *Senior Member, IEEE,* Zaheer Ahmed, *Student Member, IEEE,* and Dalma Novak, *Member, IEEE*

***Abstract*— A detailed model is developed for analyzing fiber grating external cavity lasers for both static and small-signal modulation conditions. The chip and package parasitics and leakage current induced distortion are included. The composite system is solved analytically in the small-signal regime using a Volterra functional series expansion method. As an application of the model, a thorough analysis of the appearance of nulls close to the harmonics of the cavity resonance frequency in the noise and modulation spectra is given. We show that the appearance of these nulls can be explained using the interplay of amplitude and phase coupling between laser diode and external resonant cavity. A signal flow graph approach is introduced which identifies methods of minimizing the nulls.**

***Index Terms*— External cavity, fiber Bragg grating, modeling modulation, noise, seimconductor lasers.**

## I. Introduction

THE PERFORMANCE of semiconductor laser diodes is significantly affected by the existance of intentional [1]–[3] or unintentional [4], [5] feedback from passive external reflectors. It has been shown experimentally that optical feedback has a strong influence on the :

1) threshold current [3];
2) the steady state output power [1], [2], [6];
3) stimulated and noise emission spectra [7], [8];
4) linear and nonlinear dynamics of the laser [8]–[10].

Tkach and Chraplyvy [11] were one of the first groups to carry out a detailed experimental study of the effect of external feedback on semiconductor lasers, ranging from weak ($< -40$ dB) to strong ($> -10$ dB) feedback levels. Besnard *et al.* [12] extended this study to include low-frequency self-pulsations, generation of subharmonics of the modulated injection current and splitting of peaks in the modulated spectrum close to the external cavity resonance frequency (ECRF). These experiments showed that there are five phenomenologically distinct operating regimes, ranging from weak to strong feedback levels. The first four regimes are for weak to moderate feedback levels, where feedback was seen as a perturbation on the intrinsic diode lasing field. A wealth of dynamics ranging from RIN suppression to coherence collapse in a chaotic state has been observed within these feedback levels [10]. In the fifth regime, strong external feedback is used to control the lasing medium. These studies showed that feedback from a highly frequency-selective external cavity leads to stable, single mode operation. Experimentally it was also shown that these lasers are stable over further extraneous secondary feedback [11]. This led to the increase in research on strong feedback external cavity (SFEC) lasers for optical communication systems. Several SFEC frequency selective schemes have been reported in literature, including:

1) feedback from a grating [13];
2) feedback from a high-$Q$ narrow-band resonator [14];
3) the feedback from a fiber Bragg grating (BG) reflector [15].

In this paper, a detailed analysis of a BG reflector based SFEC laser is presented, as BG reflectors offer a natural choice for obtaining a strong frequency-selectivity in an external cavity. However, the generality of our theoretical analysis means that it is applicable to any of the configurations given above.

Due to low coupling loss, simplicity of packaging, thermal stability and low manufacturing cost, fiber grating external cavity (FGEC) lasers [15]–[18] have attracted much attention as sources in wavelength-division-multiplexed fiber-optic communication systems. In 1982, Sullivan *et al.* [16] proposed FGEC lasers as a means of improving the performance of solitary FP laser diodes. A detailed experimental investigation of the above proposal was carried out by Hammer *et al.* [17]. They demonstrated that FGEC lasers could maintain single mode operation over a wide range of injection currents and temperatures. However, due to the reduction of the small-signal bandwidth in FGEC lasers as a result of the increase in photon lifetime in the external cavity, these lasers were not considered useful as directly modulated laser transmitters. Therefore, until recently, FGEC lasers found use only in mode-locking [19] and tunable source applications. However, there is currently a growing amount of research in the direct modulation of external cavity lasers for generating high-efficiency microwave and millimeter-wave modulated light for applications such as optical feeds and control of phased-array radars [20] and narrow-band subscriber multiplexed (SCM) systems [21]–[23]. The advantage of external cavity lasers over conventional solitary lasers can be explained by noting that, due to resonance-enhancement [23], external cavity lasers can be modulated at frequencies much higher than the intrinsic bandwidth of solitary laser diodes [24]–[26].

Many theoretical models for quantum noise and modulation response of lasers with feedback have been described in the literature. However many of these models concentrate only on weak feedback conditions. Ferreirera *et al.* [8] were the first to conduct a detailed study of both noise and modulation

Manuscript received November 18, 1996; revised February 18, 1997.

The authors are with The Australian Photonics Cooperative Research Centre, Photonics Research Laboratory, Department of Electrical and Electronic Engineering, The University of Melbourne, Parkville, VIC 3052, Australia.

Publisher Item Identifier S 1077-260X(97)04509-7.

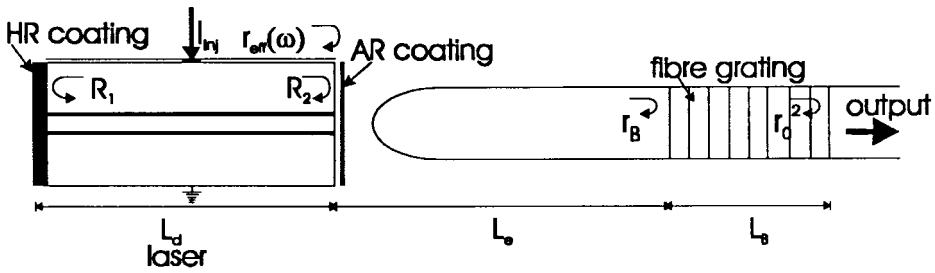


Fig. 1. Schematic diagram of FGEC laser. AR: antireflective coating; HR: high-reflective coating.

performance under strong feedback conditions. However, their treatment underestimated the importance of including retarded field components to represent the significant external cavity delay. They also excluded chip and package parasitics and nonlinear distortion effects. Recently, several other groups have conducted research on strong feedback induced effects such as bistability, self-pulsations and anomalous spectral behavior including subharmonic generation and the appearance of narrow peaks centered around the harmonics of the cavity resonance in noise and modulation spectra [6], [7], [27]. These studies emphasised the importance of multiple reflections under strong feedback conditions. By considering multiple reflections and finite-delay effects due to passive, frequency selective feedback, Ahmed *et al.* [27] analyzed the spectral splitting of the intensity modulation (IM) response close to the ECRF. However, their theoretical study was not self consistent as they did not solve the steady-state equations, simultaneously satisfying gain and round-trip phase conditions. Thus, their theoretical treatment can be taken only as a qualitative guide for explaining the experimental results. Ahmed *et al.* [27] also excluded noise and nonlinear distortion in their theoretical work. Extending a laser model developed by Glasser [28], Nagarajan *et al.* [29] developed a detailed analytical model for explaining noise and modulation response under strong signal feedback conditions. They used a simplified perturbation analysis to take nonlinear distortion effects into account. However, they ignored the effects of residual intermediate facet reflectivity in their analysis.

In this paper, we develop a detailed model which can characterize fiber grating external cavity (FGEC) lasers including packaging parasitics, leakage current induced distortion [30], and intrinsic linear and nonlinear effects resulting from carrier–photon interactions [31]. Our approach is based on the rate equations and is an extension of the multiple reflection, strong feedback model given by Park *et al.* [32]. Following the treatment of Rong-Qing *et al.* [33], multiple reflections are handled compactly using an assumption of stationarity of the field components. By stationarity, we imply that the outcome is independent of the time reference. The validity of this stationarity argument can be justified by noting that our analysis is only restricted to periodic and nonperiodic steady state conditions. However, the treatment of Rong-Qing *et al.* [33], failed to recognize the importance of delayed laser field amplitude and phase components after multiple reflections and these were replaced with first order differentials. By retaining the delayed laser field amplitudes and phases after multiple reflections, we extend our analysis to comparatively longer cavities and also retain the delay induced interference effects, which we show to be critical in predicting peaks and nulls. To characterize the leakage current induced nonlinear effects associated with fabrication architecture, a homo-junction diode-leakage-current model [30] is used. By considering the linear and nonlinear loading effects, the linear parasitic model is modeled as a nonlinear Volterra model [31]. Previous detailed studies by Nagarajan *et al.* [25], and Ahmed *et al.* [27], have excluded loading effects.

This paper is organized as follows: In Section II, we present the detailed theoretical modeling of FGEC lasers, including parasitcs and leakage current effects. In Section III, we use this model to analyze the resonance spectral peak splitting in noise and modulation spectra of FGEC lasers. In this section a signal flow graph approach is introduced to explain the appearance of nulls in the noise spectrum and modulation response. Section IV will summarize the results and conclude the paper.

## II. Analytical Model

A schematic diagram of the device under consideration is shown in Fig. 1. It consists of a Fabry–Perot (FP) laser diode with high reflectivity (HR) and antireflective (AR) coated facets. The light from the AR coated facet is coupled to the fiber Bragg grating reflector. The output power is taken through the grating. The grating reflectivity is kept low (i.e., Bragg grating normalized coupling strength $\leq 1$) to ensure a reasonably high output power. Fig. 2(a) shows the equivalent circuit model for this device. The package parasitics and leakage current models are considered in cascaded functional form with an intrinsic composite-cavity laser model to ease the modeling task. We develop separate Volterra functional models [31] for each of these and cascade them to obtain the third-order Volterrra functional model as shown in Fig. 2(b).

### A. Intrinsic Composite Cavity Laser Model

Experimental studies with strong-feedback external cavity lasers have shown that they can maintain strong, stable-single mode operation, even under high power operation [34]. The reason for strong, stable single-mode operation is easily justified for external mirrors having bandwidths narrower than the external cavity mode spacing. However, Doerr *et al.* [35] have recently shown that these results hold even for lasers with an external mirror having a bandwidth of a few external cavity modes. They showed that mode beating between adjacent modes transfers power between the modes, leading to a central, dominant mode. The dynamical aspects of this mode selection under wave mixing effects in semiconductor amplifiers have also been investigated in

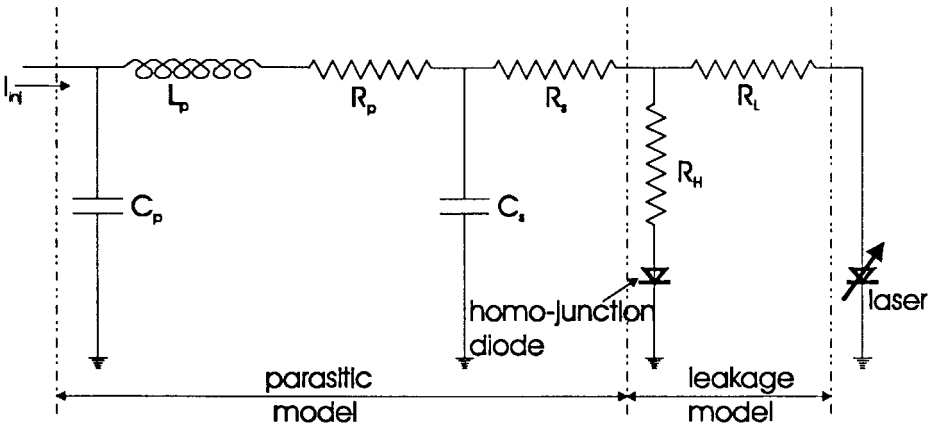


(a)

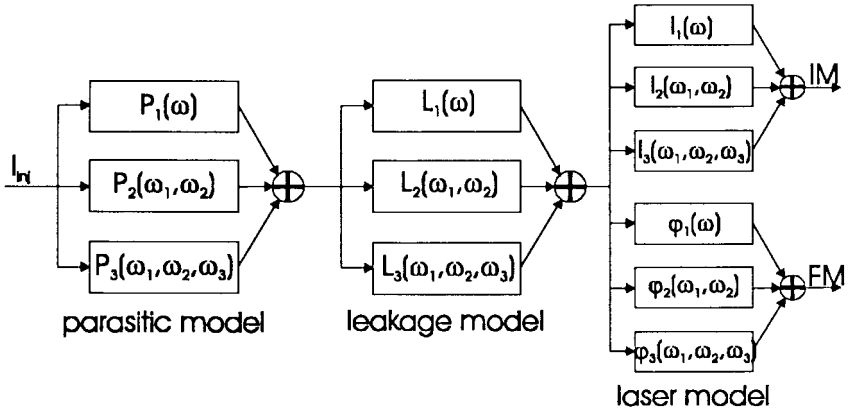


(b)

Fig. 2. (a) The equivalent circuit model representation of FGEC laser. (b) Circuit representation is modeled as Volterra functional model. Subscripts under the transfer functions denote the Volterra functional order.

detail [36]. However, we believe that the actual mechanism responsible for this experimentally observed strong, single mode operation needs to be further studied in detail before any conclusion can be reached. Considering above reasons, we limit our study to the single mode case, however the multimode case will be investigated in future work.

Considering the multipass, strong feedback from the grating reflector, the following equations can be used to characterize the temporal evolution of the lasing-dynamical system [32]:

$$\frac{dI}{dt} = (aV_gH(\omega)(N-N_t)/\sqrt{1+2\epsilon I} - \alpha_L + \ln(R_1R_2)\tau_L)I + 2(\mathrm{Re}(\ln(f))/\tau_l)I \quad (1)$$

$$\frac{d\varphi}{dt} = (\varpi - \omega_s) + 0.5\alpha_{\mathrm{gsp}}(\Gamma aV_gH(\omega)(N-N_t) - \alpha_L + \ln(R_1|R_{\mathrm{eff}}|)/\tau_L) + \mathrm{Im}(\ln(f))/\tau_L \quad (2)$$

$$\frac{dN}{dt} = \frac{i_{\mathrm{inj}}}{qV} - (AN + BN^2 + CN^3) - (\Gamma aV_g(N-N_t)/\sqrt{1+2\epsilon I})I \quad (3)$$

where $I$ is the spatially averaged intensity of the lasing field, $\varphi$ is the phase of the lasing field and $N$ is the carrier density in the active region. Descriptions of the other parameters used in these equations are given in Table I. Park *et al.* [32] and Ahmed *et al.* [27] have used similar set of equations to describe external cavity lasers, however, we have also incorporated the spectral profile of the gain $H(\omega)$. We have used a Lorenzian profile for $H(\omega)$ and ignored the carrier density dependence of the gain-peak wavelength. The details of $H(\omega)$ can be found in reference [37]. The importance of the incorporation of $H(\omega)$ can be seen by noting that the side-mode suppression ratio in FGEC lasers depends significantly on the detuning between the peak wavelength in the gain spectrum and the Bragg wavelength of the fiber grating [37]. As these lasers are capable of operating single mode at high powers [34], we have introduced the modified gain saturation term of the form $\sqrt{1+2\epsilon I}$. Using a quantum mechanical density matrix approach, Agrawal [38], [39] showed that this form of gain saturation term is more realistic compared with the conventional form, $(1+\epsilon I)$, although it is clear that these two forms deviate significantly from each other only at high powers. In our model, the external cavity effects were modeled using the lumped feedback parameter, $f$. Considering multipass reflections in the external cavity, $f$ can be given in the following form [32], [33]:

$$f(\omega) = 1 + \hat{C}\frac{r_{\mathrm{Bragg}}}{\sqrt{R_2}}(1-R_2)\sum_{n=1}^{\infty}\sqrt{\frac{I(t-n\tau)}{I(t)}} \cdot (-\sqrt{R_2}r_{\mathrm{Bragg}})^{n-1} \cdot \exp(-j\omega n\tau + j(\varphi(t-n\tau) - \phi(t))) \quad (4)$$

where $r_{\mathrm{Bragg}}$ is the field reflectivity of the Bragg grating seen by the external cavity field. $r_{\mathrm{Bragg}}$ can be calculated

using coupled mode theory [40]. It is important to note that (1)–(4) do not diverge as $R_2$ tends to zero, though the individual definitions seem to diverge. This can be understood by observing that in (1), the term $\ln(R_1R_2)/\tau_L + 2\ \mathrm{Re}(\ln(f))/\tau_L$ reduces to $\ln(R_1|R_{\mathrm{eff}}|)/\tau_L$ and in (2) the term $\mathrm{Im}(\ln(f))/\tau_L$ reduces to $\mathrm{Im}(\ln(r_{\mathrm{eff}}))/\tau_L$. The parameter $r_{\mathrm{eff}} = \sqrt{R_{\mathrm{eff}}}\exp(j\arg(r_{\mathrm{eff}})) = \sqrt{R_2}f$ is the effective reflectivity of the external cavity seen from the laser diode. Assume that the longitudinal, effective–refractive index variation of the Bragg grating is given as [41],

$$n_B(z) = n_{BO} + \Delta n_B \cos\left(\frac{2\pi}{\Lambda_B}z + \vartheta_B\right) \tag{5}$$

where $n_{BO}$ is the unperturbed effective index of the fiber, $\Delta n_B$ is the index-perturbation-amplitude of the fiber, $\Lambda_B$ is the grating corrugation period and $\vartheta_B$ is the grating phase at $z = 0$. Due to this periodic corrugation, the forward-propagating laser field $E^+$ is coupled to the back-propagating laser field $E^-$, though Bragg diffraction. Using coupled mode theory [40], the inter-coupling relations between $E^+$ and $E^-$ can be written as

$$\frac{dE^+}{dz} = -\left(\frac{\alpha_B}{2} + j\delta\right)E^+ - j\kappa e^{-j\vartheta}E^- \tag{6}$$

$$\frac{dE^-}{dz} = \left(\frac{\alpha_B}{2} + j\delta\right)E^- + j\kappa e^{j\vartheta}E^+ \tag{7}$$

where $\alpha_B$ is the loss coefficient for power in Bragg grating, $\kappa$ is the coupling strength and $\delta$ is the detuning of the incident wave frequency from Bragg condition, given by $\delta = (\omega n_{BO}/c - \pi/\Lambda_B)$.

This set of equations can be solved analytically to obtain the reflectivity of the Bragg grating seen from the external cavity; noting $r_{\mathrm{Bragg}} = (E^+/E^-)_{Z=0}$, we get (8), found at the bottom of the page [41], where $\beta_B = \pi/\Lambda_B, \gamma_B^2 = (\alpha_B/2 + j\delta)^2 + \kappa^2$ and $r_0^2$ is the reflectivity of the grating to fiber coupling interface as shown in Fig. 1. Noting that $r_{\mathrm{Bragg}}$ is a complex quantity, it can be written in a polar form, $r_{\mathrm{Bragg}} = |r_{\mathrm{Bragg}}|\exp(j\angle r_{\mathrm{Bragg}})$. The magnitude $|r_{\mathrm{Bragg}}|$ gives the frequency dependent reflectivity, while the phase $\angle r_{\mathrm{Bragg}}$ induces different delays (i.e., delay $= (\partial/\partial\omega)(\angle r_{\mathrm{Bragg}})$) to the reflected field, depending on the incident frequency. This leads to the change of effective cavity length with frequency and hence the cavity resonance frequency. We have taken this effective length variation of the external cavity and the carrier density dependent variation of the solitary laser effective laser length into account in our analysis for the accurate interpretation of results.

Although our analysis is limited to uniform gratings, it is interesting to consider chirped gratings as well. Chirping will lead to the modification of amplitude and phase response of the Bragg grating's reflectivity. However, for typical gratings with around 0.1-nm bandwidth, this modification can only be expected to affect the steady state operating point because the grating's frequency selectivity is low compared with the modulation frequency. It has been shown experimentally that chirp improves the stability of the steady state oscillating mode, for certain chirp-orientations [34]. However the qualitative aspects of the modulation response is not expected to change significantly relative to uniform gratings with similar bandwidths for high speed modulation. This can be understood by considering that due to small signal modulation, the operating point on the grating is not going to be changed significantly for a grating having a bandwidth of the order of 0.1 nm. However this result is expected to change for long-chirped gratings (∼10 cm) as the bandwidth will become significantly small. The issues of dynamic modulation stability become important for long gratings. Therefore the small signal analysis given here is not adequate for the analysis of these gratings. Work is in progress to modify the current model to analyze these lasers with long-chirped gratings.

To analyze the above set of equations in the small signal regime, we carry out a perturbation analysis around a steady state oscillation mode. Steady-state solutions can be found by solving the above equations self-consistently, considering gain and round-trip phase conditions. However, due to the large parametric space associated with these equations, perturbation expansion around the steady-state solution introduces unwieldy and complex expressions for further manipulation. Therefore, to simplify the task, we introduce the notation given in Table II. Using these axiomatic operators, and expanding (1)–(8) around an oscillating mode, and retaining up to third-order terms, we obtain the following set of equations:

$$\begin{aligned}\partial|1\rangle = &\sum_{\alpha=1-3}\left\{\frac{\wp(1]}{\wp\lfloor\alpha]}|\alpha\rangle + \frac{\wp(1]}{\wp\lfloor 1\alpha]}|1\alpha\rangle\right\} \\ &+ \sum_{\alpha=1,3}\left\{\frac{\wp(1]}{\wp\lfloor\alpha\partial 2]}|\alpha\partial 2\rangle + \frac{\wp(1]}{\wp\lfloor 1\alpha\partial 2]}|1\alpha\partial 2\rangle\right\} \\ &\cdot \sum_{\alpha=1,2}\frac{\wp(1]}{\wp\lfloor\Diamond_\tau\alpha]}|\Diamond_\tau\alpha\rangle + \frac{\wp(1]}{\wp\lfloor\partial 2]}|\partial 2\rangle \\ &+ \frac{\wp(1]}{\wp\lfloor\Diamond_\tau 2]}|\Diamond_\tau 2\rangle + \frac{\wp(1]}{\wp\lfloor 113]}|113\rangle + |L_1\rangle \end{aligned} \tag{9}$$

$$\begin{aligned}\partial|2\rangle = &\sum_{\alpha=1-3}\frac{\wp(2]}{\wp\lfloor\alpha]}|\alpha\rangle + \sum_{\alpha=1,2}\frac{\wp(2]}{\wp\lfloor\Diamond_\tau\alpha]}|\Diamond_\tau\alpha\rangle \\ &+ \frac{\wp(2]}{\wp\lfloor\partial 2]}|\partial 2\rangle + \frac{\wp(2]}{\wp\lfloor 3\partial 2]}|3\partial 2\rangle + \frac{\wp(2]}{\wp\lfloor 11]}|11\rangle \\ &+ \frac{\wp(2]}{\wp\lfloor 1\Diamond_\tau 1]}|1\Diamond_\tau 1\rangle + |L_2\rangle \end{aligned} \tag{10}$$

$$\begin{aligned}\partial|3\rangle = &\frac{\wp(3]}{\wp\lfloor 0]} + \sum_{\alpha=1,3}\left\{\frac{\wp(3]}{\wp\lfloor\alpha]}|\alpha\rangle + \frac{\wp(3]}{\wp\lfloor\alpha\alpha]}|\alpha\alpha\rangle \right. \\ &\left. + \frac{\wp(3]}{\wp\lfloor\alpha\alpha 3]}|\alpha\alpha 3\rangle\right\} + \frac{\wp(3]}{\wp\lfloor 13]}|13\rangle + |L_3\rangle \end{aligned} \tag{11}$$

$$r_{\mathrm{Bragg}} = \frac{r_0\exp(-j(2\beta_BL_B + \vartheta_B))(\gamma_B\cosh(\gamma_BL_B) - (\alpha_B/2 + j\delta)\sinh(\gamma_BL_B)) - j\kappa\sinh(\gamma_BL_B)}{\gamma_B\cosh(\gamma_BL_B) + ((\alpha_B/2 + j\delta) + j\kappa r_0\exp(-j(2\beta_BL_B + \vartheta_B)))\sinh(\gamma_BL_B)} \tag{8}$$

TABLE I
FGEC LASER PARAMETERS

| Parameter | Description | Value | | Units |
|---|---|---|---|---|
| $c$ | speed of light in vacuum | $3.0\times10^{8}$ | | $ms^{-1}$ |
| $q$ | electron charge | $1.602\times10^{-19}$ | | C |
| $h$ | Plank's constant | $6.626\times10^{-34}$ | | $Js^{-1}$ |
| $k$ | Boltzmann constant | $1.381\times10^{-23}$ | | $JK^{-1}$ |
| $L$ | solitary laser diode length | 300.0 | | μm |
| $W$ | solitary laser diode width | 2.0 | | μm |
| $D$ | solitary laser diode depth | 0.2 | | μm |
| $V$ | volume of the solitary laser=($LWD$) | $1.2\times10^{-16}$ | | $m^3$ |
| $L_e$ | external cavity length | ##, #* | | m |
| $L_g$ | fibre Bragg grating length | 8.0 | | mm |
| $\Lambda_g$ | Bragg grating period | 516.33 | | nm |
| $\kappa L_g$ | normalised coupling strength of grating | 1.0 | | |
| $n_{g0}$ | effective index of the fibre | 1.5 | | |
| $n_e$ | effective index | 3.4 | | |
| $n_g$ | group index | 3.4 | | |
| $\hat{C}$ | feedback coupling efficiency | 1.0 | | |
| $V_g$ | group velocity of light in laser medium | $8.824\times10^{7}$ | | $ms^{-1}$ |
| $\alpha_{sp}$ | linewidth enhancement factor | ## | | |
| $\alpha_L$ | scattering loss | 3000.0 | | $m^{-1}$ |
| $\alpha_g$ | grating power-loss coefficient | 0.0 | | $m^{-1}$ |
| $\Gamma$ | field confinement factor | 0.20 | | |
| $a$ | gain cross section | $2.5\times10^{-20}$ | | $m^2$ |
| $\lambda_p$ | gain peak wavelength | 1549.0 | | nm |
| $\Delta\lambda_p$ | gain spectral width | 30.0 | | nm |
| $A$ | mono-molecular recombination coeff. | $1.0\times10^{8}$ | | $m^3s^{-1}$ |
| $B$ | bi-molecular recombination coeff. | $8.0\times10^{-17}$ | | $m^6s^{-s}$ |
| $C$ | Auger recombination coeff. | $7.5\times10^{-41}$ | | $m^9s^{-1}$ |
| $R_1$ | reflectivity of HR coated facet | 0.9025 | | |
| $R_2$ | reflectivity of the intermediate facet | ## | | |
| $r_0^2$ | grating-fibre interface reflectivity | 0.0 | | |
| $n_{sp}$ | population inversion parameter | 2.2 | | |
| $\varepsilon$ | gain saturation factor | $1.0\times10^{-23}$ | | $m^3$ |
| $N_t$ | transparency carrier density | $1.2\times10^{24}$ | | $m^{-3}$ |
| $I_{inj}$ | injection current | ## | | A |
| $C_p$ | bond-wire capacitance | 0.23 | | pF |
| $L_p$ | bond-wire inductance | 0.25 | | nH |
| $R_p$ | bond-wire resistance | 2.5 | | Ω |
| $C_s$ | shunt capacitance | 15.0 | | pF |
| $R_s$ | series chip resistance | 10.0 | | Ω |
| $R_H$ | homo-junction diode,series resistance | 1.0 | | Ω |
| $R_L$ | laser diode resistance in leakage model | 0.2 | | Ω |
| $\eta$ | homo-junction diode inhibiting factor | 2.0 | | |
| $V_s$ | saturated, terminal voltage of the laser | 0.954 | | V |
| $T$ | laser operating temperature | 298.0 | | K |
| $I_{s0}$ | reverse saturation current of h-j. diode | #* | | A |
| $\zeta I_{s0}$ | | 6.0 | | mA |
| $\tau_D$ | diffusion time constant | $1x10^{-12}$ | | s |
| $\tau$ | external cavity round-trip time | ##, #* | | s |
| $\tau_L$ | solitary laser round-trip time | ##, #* | | s |
| $\varpi$ | laser operating angular frequency (without feedback) | | #* | rad/s |
| $\omega$ | instantaneous angular frequency(with feedback) | | #* | rad/s |

**key:**

| | |
|---|---|
| ## | these quantities are varied in calculations and given in text and in figure captions. |
| #* | these quantities are calculated using details given in text and in appendix. |
| ##, #* | combination of above two: depend on the context. |

TABLE II

Suppose $\Delta I(t)$, $\Delta\varphi(t)$ and $\Delta N(t)$ represent small fluctuations of average photon density, optical field phase and average carrier density from an unperturbed state. We introduce following mapping relations to represent, actual mode statistics:

$$|1\rangle = |1(t)\rangle = V\Delta I(t), \qquad |2\rangle = |2(t)\rangle = \Delta\varphi(t), \qquad |3\rangle = |3(t)\rangle = \Gamma V\Delta N(t)$$

and postulate the following relations:

$$1 = |0\rangle$$
$$|\alpha\beta\rangle = |\alpha\rangle|\beta\rangle, \ \forall\alpha,\beta$$
$$\Diamond_\tau|\alpha\rangle = |\Diamond_\tau\alpha\rangle = |\alpha(t-\tau)\rangle, \ \forall\alpha$$
$$\partial|\alpha\rangle = |\partial\alpha\rangle = \frac{d|\alpha\rangle}{dt}, \ \forall\alpha$$
$$\langle\alpha| = |\alpha^*\rangle = |\alpha\rangle^*, \ \forall\alpha$$

and replace the coefficients associated terms of the form $|\alpha\cdots\beta\rangle$ in first order differential relations of the form $\{\partial|\gamma\rangle = \cdots + coeff\cdot|\alpha\cdots\beta\rangle + \cdots\}$ with more descriptive, differential like form:

$$\frac{\wp[\gamma]}{\wp[\alpha\cdots\beta]} = coeff$$

Circular-Sum is defined for generally, non-commutable functional arguments of the form $\Pi(\alpha_1\cdots\alpha_k)\cdots\Pi(\alpha_p\cdots\alpha_r)$, with $(1\leftrightarrow S)$ circularly arranged arguments as:

$$\underset{(\alpha_k\ldots\alpha_s)}{\overset{(1,\ldots S)}{\prec}}\Pi_1(\alpha_1,\ldots\alpha_k)\cdots\Pi_q(\alpha_p,\ldots\alpha_S) = \sum\Big[function\ value\ at\big(\big(\alpha_{1,\ldots}\alpha_s\big) = circularly\ permuted(1,\ldots S)\big)\Big]$$

eg: $\underset{(\alpha,\beta,\gamma)}{\overset{(a,b,c)}{\prec}} f(\alpha)g(\beta,\gamma) = f(a)g(b,c) + f(b)g(c,a) + f(c)g(a,b)$

where Langevian forces $\{|L_\alpha\rangle{:}\alpha \in (1-3)\}$ represent the random fluctuations of intensity, phase and carrier density, respectively [42]. The associated, quantum-mechanically calculated auto- and cross-correlation relations for these forces can be written as [42]:

$$\langle\langle L_1(t)|L_1(t-\zeta)\rangle\rangle = R(2I_s+1)\delta(\zeta)$$
$$\langle\langle L_1(t)|L_2(t-\zeta)\rangle\rangle = \langle\langle L_2(t)|L_1(t-\zeta)\rangle\rangle = 0 \tag{12}$$
$$\langle\langle L_2(t)|L_2(t-\zeta)\rangle\rangle = \frac{R}{2I_s}\,\delta(\zeta)$$
$$\langle\langle L_2(t)|L_3(t-\zeta)\rangle\rangle = \langle\langle L_3(t)|L_2(t-\zeta)\rangle\rangle = 0 \tag{13}$$
$$\langle\langle L_3(t)|L_3(t-\zeta)\rangle\rangle = R\delta(\zeta)$$
$$\langle\langle L_1(t)|L_3(t-\zeta)\rangle\rangle = \langle\langle L_3(t)|L_1(t-\zeta)\rangle\rangle = -R\delta(\zeta) \tag{14}$$

where $R$ is the spontaneous emission rate into the cavity and $\delta(\zeta)$ is the Dirac delta function. The detailed expressions of the perturbation expansion coefficients are given in Appendix A1. Using the harmonic-probing method [43], the Volterra functional representation for (9)–(11) has been calculated and is given in Appendix A2.

*1) Intensity Noise:* The resonance of the external cavity also enhances the relative intensity noise (RIN) around the desired modulation frequency, leading to reduction of the sensitivity in the optical receiver [29]. A qualitative and quantitative understanding of RIN performance is therefore vital. The RIN is defined as the ratio of the mean square intensity fluctuation to the mean intensity squared of the laser output [29]. Using the first kernel of the Volterra functional

expansion, the spectral density of the RIN can be written as

$$\mathrm{RIN}(\Omega) = \frac{R}{|\det(\Im_1^\Omega) I_S|^2} \left(2I_S|\Im_{122}^\Omega \Im_{133}^\Omega|^2 + |\Im_{122}^\Omega \Im_{133}^\Omega - \Im_{112}^\Omega \Im_{123}^\Omega + \Im_{113}^\Omega \Im_{122}^\Omega|^2 + |\Im_{112}^\Omega \Im_{133}^\Omega|^2/2I_S\right) \tag{15}$$

where matrix $\Im_1^\Omega = \{\Im_{1\alpha\beta}^\Omega \colon \alpha, \beta \in \{1,2,3\}\}$ represents the value of matrix $\Im_1(\omega)$, evaluated at angular frequency $\Omega$ (see Appendix A). The behavior of this expression is studied later for the detailed characterization of the resonance-peak spectral splitting phenomena.

### *B. Modeling of Parasitics and Leakage Current*

Intermodulation distortion (IMD) in semiconductor lasers has long been recognized as a significant performance limiting factor in subcarrier multiplexed systems [44] and is mainly due to two effects [29]:

1) intrinsic nonlinearity in the carrier-photon interactions;
2) leakage currents and nonlinear loading of parasitics.

We modeled leakage current effects by incorporating a homojunction diode in parallel with the intrinsic laser model. Lin *et al.* [30] have given a thorough account on the validity of this model. Considering the frequency dependency of the nonlinear leakage current model, Volterra functional representations have been calculated and are given in Appendix B. Appendix C gives a Volterra functional representation of the parasitic circuit [see Fig. 2(a)] [45]. Although a linear model has been considered for the parasitics, the appearance of second and third order Volterra kernels can be explained by noting the nonlinear loading of the intrinsic laser and homojunction diode models.

### *C. Small-Signal IM and IMD Response of the Combined Model*

The carrier density, photon density and optical field phase exhibit complex dynamics governed by the rate equations (9)–(11) and parasitic and leakage current model responses. Periodical modulation leads to the synchronization of these dynamics. Fig. 2(b) shows the equivalent Volterra transfer-function representation of the combined model. Using Volterrra transfer-function cascading theorems [46], we reduce this system to an equivalent effective transfer-function form with first, second and third-order Volterra kernels: $T_1(\omega), T_2(\omega_1, \omega_2)$ and $T_3(\omega_1, \omega_2, \omega_3)$, respectively. Assuming that the photon density to power conversion factor through the fiber grating is $\Re$, the IM (Intensity Modulation) response of the combined system can be given as

$$\mathrm{IM}(\Omega) = \Re T_1(\Omega) \tag{16}$$

where $\Omega$ represents the modulation angular-frequency. Under resonant modulation schemes, the dominant distortion to the IM results from third order intermodulation products falling within the transmission band. Quantitative measures of the magnitude of this distortion can be obtained by calculating the IMD relative to the carrier, $C$. Adopting the criteria used by Nagarajan *et al.* [29], we can obtain the following expression for the IMD response relative to the carrier, $C$:

$$\frac{\mathrm{IMD}(\Omega)}{C} =_{|\Delta\Omega/\Omega| \ll 1} \Re m^2 (\overline{I}_{\mathrm{inj}} - I_{\mathrm{th}})^2 \cdot (0.75 T_3(\Omega - \Delta\Omega, \Omega - \Delta\Omega, -\Omega) + 15 T_3(\Omega - \Delta\Omega, \Omega, -\Omega - \Delta\Omega))/T_1(\Omega) \tag{17}$$

where $\overline{I}_{\mathrm{inj}}$ is the average injection current, $I_{\mathrm{th}}$ is the threshold current, and $m$ is the modulation index.

## III. Resonance-Peak Spectral Splitting (RPSS)

As an application of the developed model, we investigate the appearance of narrow nulls close to harmonics of the cavity resonance frequency in noise and modulation spectra of FGEC lasers. This "Resonance-peak spectral splitting (RPSS)" characteristic has been reported by many researchers in the past [12], [27], [47], [48]. Sato *et al.* [47] and Besnard *et al.* [12] suggested that the excitation of multimodes to be the origin of these results. By carrying out detailed theoretical and experimental investigations, Port *et al.* [48] argued that complex relaxation phenomena lead to the observed splitting. Recently, Ahmed *et al.* [27] conducted extensive theoretical and experimental studies to characterize RPSS in directly modulated grating-coupled external cavity lasers. They related the resonance-peak splitting in IM response to the resonance-peak splitting in RIN, and explained the RIN spectral splitting as being due to two processes:

1) the translation of low-frequency RIN to high-frequency RIN through beating with the high-frequency modulation signal;
2) the resonant enhancement of the relaxation oscillation magnitude.

Our analysis of RIN, however, shows that such beating between low-frequency RIN and high-frequency modulation does not need to be present for the appearance of RPSS. In this section, we give conclusive evidence to show that RPSS in noise and modulation spectra result from the complex amplitude-phase coupling interplay between active and passive resonant cavities.

### *A. IM and RIN Spectra*

We use the data given in Table I for our simulations. The steady-state light versus current ($L$–$I$) characteristic is given in Fig. 3. This has been calculated by simultaneously solving (1)–(3) to satisfy gain and round-trip phase conditions for the combined cavity. Because we obtain multiple solutions corresponding to possible lasing modes, an optimization algorithm is used to select the mode with the lowest threshold gain (i.e., the lasing mode). Fig. 3 shows a predominantly linear $L$–$I$ characteristic with some irregularity resulting from the mode-hopping between external cavity modes. The mode hopping can be easily seen in the numerical solution of (1)–(3). The oscillation frequency is a smooth function of bias current due to the change in the refractive index of the active section. However, if this change in frequency is sufficiently large, the mode frequency is pulled to the next cavity mode, which causes mode hopping. Morton *et al.*

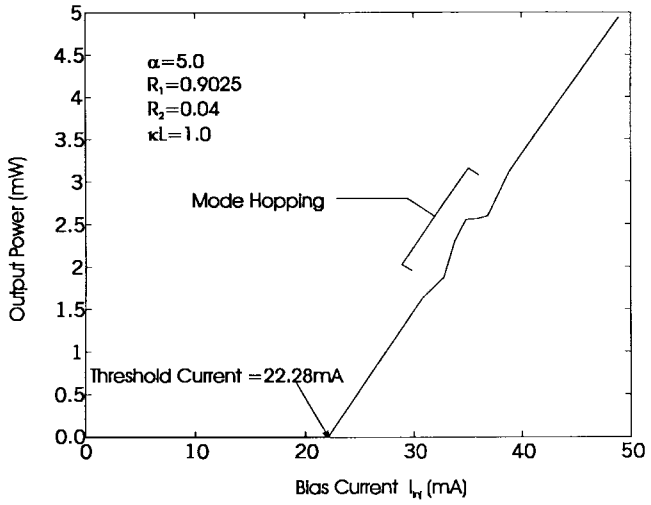


Fig. 3. The $L$–$I$ characteristics of FGEC laser with 4-GHz external cavity. Table I gives the data used for this simulation.

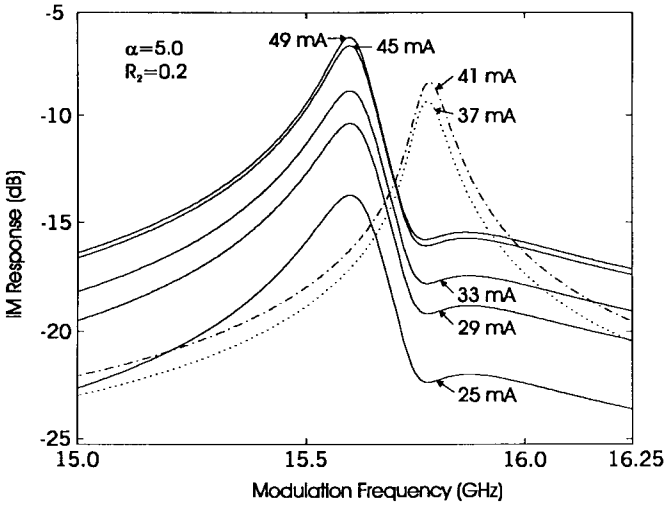


Fig. 5. IM response of pseudospectral peaks around the 4th cavity resonance harmonic. Label is bias current (4-GHz external cavity).

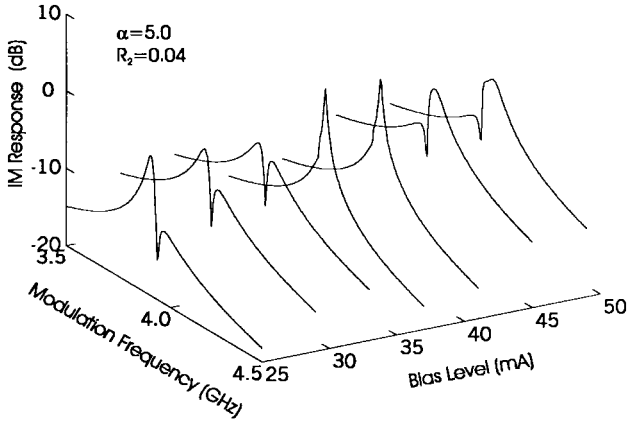


Fig. 4. Change of RPSS versus bias current. Note the splitting position variation with bias current (4-GHz external cavity).

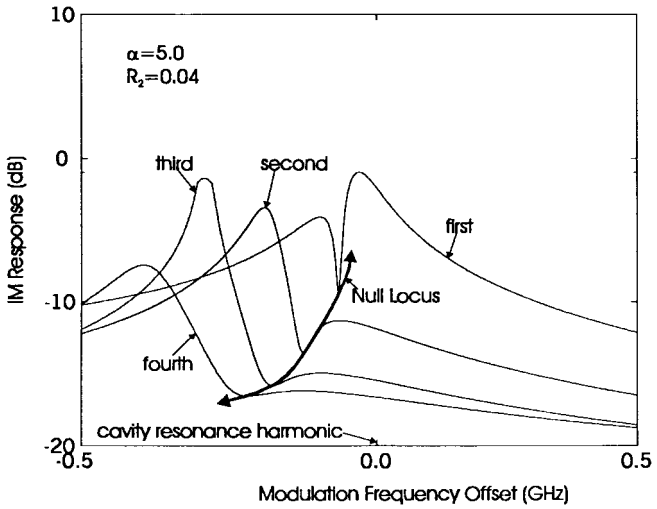


Fig. 6. IM response against frequency offset around cavity resonance harmonics. Label is harmonic number.

[19] have reported experimental results showing similar $L$–$I$ characteristics. Fig. 4 shows the variation of RPSS position in the IM response for the fundamental resonance of the 4-GHz cavity considered above. It shows that by varying the injection level, the null can be positioned anywhere on the resonance peak, and the null moves from one side of the peak to the other in the vicinity of the mode hopping region. Similar behavior has also been observed experimentally [49]. Fig. 5 shows the IM response around the 4th harmonic of the cavity resonance frequency versus bias current. The null is on the high-frequency side of the peak both above and below the mode-hopping region. Similar trends have been detected experimentally in external cavity lasers subject to strong feedback [49]. Fig. 6 compares the spectra around four harmonics of the cavity resonance. The null moves to lower frequencies at higher harmonics and creates a dominant lower frequency peak.

Detailed analyzes by Ahmed *et al.* [27] show that large intermediate-facet reflectivity, poor coupling between active and passive cavities, and a low gain suppression factor, lead to the enhancement of RPSS. Our simulations show that, apart from the above parameters, the linewidth enhancement factor $(\alpha)$, and external cavity length $(L_e)$ have a significant effect. Fig. 7 shows the change of the form of the spectral splitting for external cavity lengths 3.75, 4.75, and 7.5 cm. It clearly shows that cavity length has a direct effect on the spectral splitting shape and depth. Later we will show that this can be attributed to the dependence of amplitude-phase coupling strength on the cavity length.

Studies by Ahmed *et al.* [27] have also shown that it is necessary to have relatively large intermediate facet reflectivity in the external cavity semiconductor laser (see Fig. 1: AR coated facet = intermediate facet) for the appearance of splitting in the external cavity resonance peaks. Our studies show that more than 20% intermediate facet reflectivity relative to the external cavity grating mirror peak reflectivity leads to noticeable RPSS, under normal operating conditions. As a rule of thumb, we classify intermediate facet reflectivity greater than 20% of external reflectivity peak as severe-splitting-

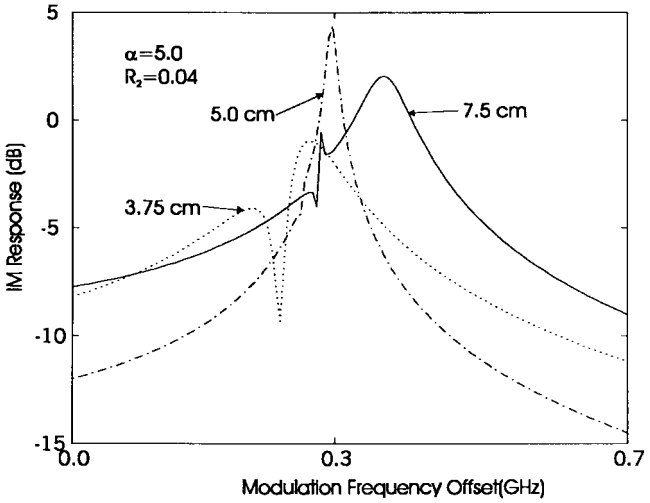


Fig. 7. IM response against modulation frequency offset for three cavity lengths. Label is the external cavity length.

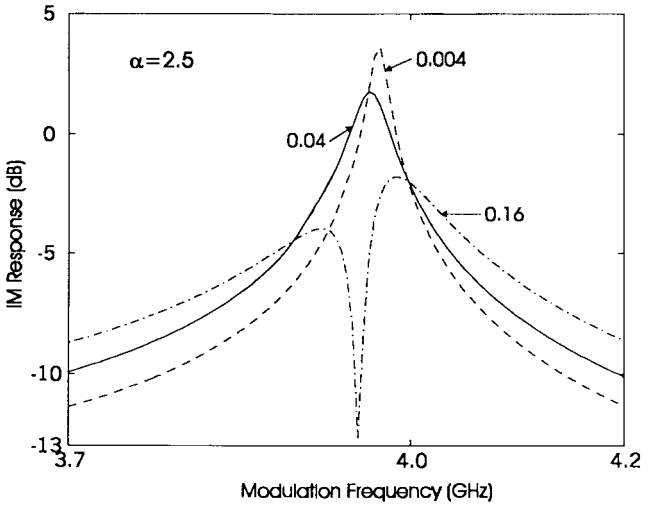


Fig. 9. IM response of the FGEC laser against modulation frequency for a fixed linewidth enhancement factor $\alpha$. Label is the intermediate facet reflectivity (4-GHz external cavity).

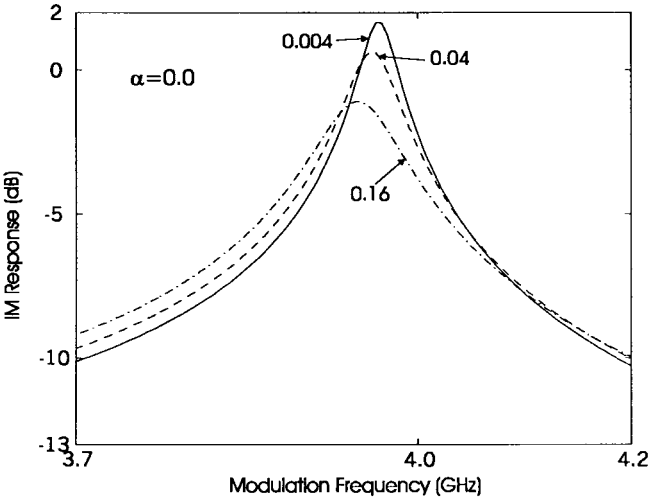


Fig. 8. IM response against modulation frequency. Label is the intermediate facet reflectivity. Same characteristics were observed for $\alpha < 1$ values (4-GHz external cavity).

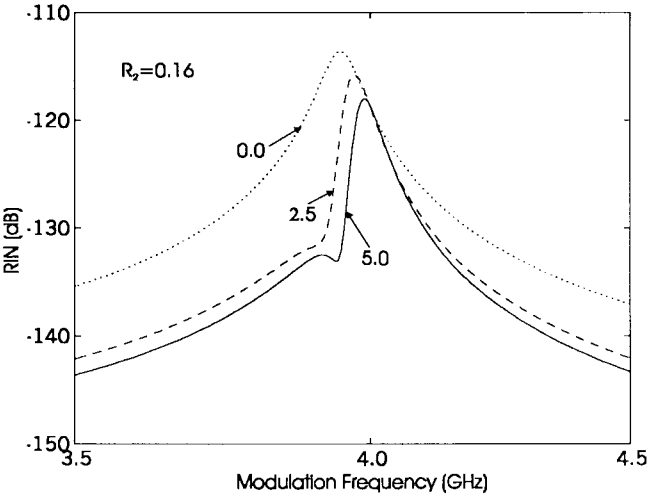


Fig. 10. RIN spectra against the frequency. Label is the linewidth enhancement factor. Similar behavior can be seen in IM response (4-GHz external cavity).

favoring (SSF) condition. To investigate the origin of spectral splitting, we analyzed the RPSS versus under severe-splitting conditions. Fig. 8 shows that when $\alpha = 0$, RPSS does not occur, although the laser is under severe-splitting-favoring conditions. Similar results were observed for $0 < \alpha < 1$. However when $\alpha$ is sufficiently high, RPSS begins to appear. This is clearly shown in Fig. 9 for $\alpha = 2.5$. Fig. 10 shows the gradual appearance of RPSS as $\alpha$ increases for a constant intermediate facet reflectivity of 0.16.

To show that the spectral splitting is due to interactions between the field amplitudes and phases in the laser and the external cavity, we developed the signal flow diagrams given in Fig. 11 (see [50] for details on signal flow graphs). Fig. 11(a) shows the inter-relationship between small-signal field amplitude, $\Delta E$, field phase fluctuation, $\Delta\varphi$, and small-signal carrier density change, $\Delta N$, for a semiconductor laser, without any external feedback. It shows that small fluctuations in the carrier density leads to small fluctuations in field amplitude. However, negative feedback due to stimulated emission modulating the carrier density tends to suppress amplitude fluctuations, especially at frequencies lower than the inverse of the carrier lifetime. The equilibrium position of these forcing and suppression actions in solitary semiconductor lasers leads to the appearance of the relaxation oscillations. Fig. 11(a) also shows that fluctuations in field amplitude and carrier density lead to fluctuations in phase or the appearance of chirp in these lasers, as is well known. However, it is interesting to note that in solitary lasers, phase fluctuations are not coupled back to amplitude or carrier fluctuations.

Now consider the introduction of strong feedback through an external resonator to this solitary semiconductor laser diode. Fig. 11(b) shows that this coupling of an external resonator to the solitary laser modifies the previously uncoupled amplitude-phase path. It shows that the external cavity introduces both self- and cross-coupling between amplitude and phase of

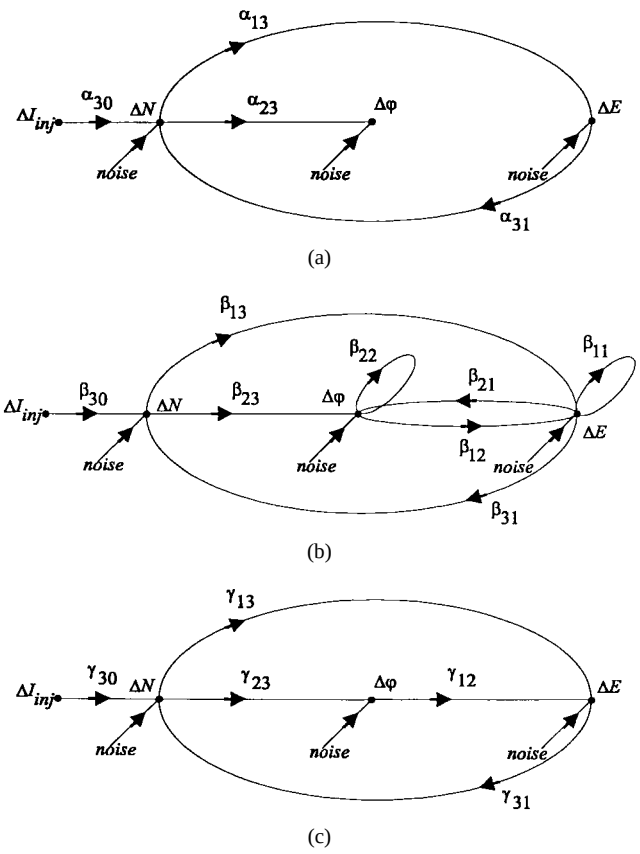


Fig. 11. Signal flow graphs relating carrier density fluctuation $\Delta N$, field amplitude fluctuation $\Delta E$ and field phase fluctuation $\Delta\varphi$. (a) Signal flow graph for solitary laser (i.e., without feedback). Note the one-way coupling to $\Delta\varphi$. (b) Signal flow graph with strong external feedback. Note the two-way cross coupling between $\Delta E$ and $\Delta\varphi$; and self-coupling in $\Delta E$ and $\Delta\varphi$. (c) Equivalent form to (b).

the lasing field. This amplitude-phase coupling through the external cavity introduce three feedback paths for any carrier fluctuation namely $\{\Delta N \rightarrow \Delta E \rightarrow \Delta N\}, \{\Delta N \rightarrow \Delta E \rightarrow \Delta\varphi \rightarrow \Delta E \rightarrow \Delta N\}$ and $\{\Delta N \rightarrow \Delta\varphi \rightarrow \Delta E \rightarrow \Delta N\}$. The equilibrium state of the fluctuations in these feedback loops represents the appearance of splitting in the resonance peaks of the noise and modulation spectra. This argument clearly establishes that significant amplitude-phase coupling is necessary for the appearance of spectral splitting. This analysis also shows that both amplitude→phase and phase→amplitude conversions need to be sustained for this to occur [see Fig. 11(a) and (b)]. Because the solitary laser is predominantly an amplitude→phase coupling device, strong phase→amplitude coupling provided through the passive external cavity is necessary to sustain a significant level of RPSS.

We also show that nonzero values of both $\alpha$ and $R_2$ are required for the amplitude-phase coupling leading to splitting in resonance peaks. Careful observation of Fig. 11(a) and Fig. 11(b) show that in the small signal regime, the effect of external feedback is to introduce two additional signal flow loops $\{\Delta N \rightarrow \Delta E \rightarrow \Delta\varphi \rightarrow \Delta E \rightarrow \Delta N\}$ and $\{\Delta N \rightarrow \Delta\varphi \rightarrow \Delta E \rightarrow \Delta N\}$ to the solitary lasing configuration. Appendix D gives the signal flow gains for the constitutive branches of these loops and shows that the cross and self coupling terms $C_C$ and $S_C$ depend explicitly on $R_2$, and implicitly on $\alpha$ through the steady state oscillation frequency. They also show that branch gains are weakly dependent on parameters such as the nonlinear gain saturation factor $\epsilon$ and external cavity length $L_e$. Numerical results show that a low value of $\alpha$ and low value of $R_2$ leads to the reduction of gains in the signal flow path $\{\Delta N \rightarrow \Delta\varphi \rightarrow \Delta E\}$. This can be clearly seen in Fig. 11(c), which is a simplified, but equivalent form of Fig. 11(b). It shows that if we eliminate the path $\{\Delta N \rightarrow \Delta\varphi \rightarrow \Delta E\}$ by making path gain negligible (i.e., by reducing $\alpha$ and $R_2$) then resonance enhancement is introduced through the frequency dependence of the path $\{\Delta N \rightarrow \Delta e \rightarrow \Delta N\}$, but the nulls disappear (see Figs. 8–10 and path gains in Appendix D). Therefore, we can clearly identify that the path $\{\Delta N \rightarrow \Delta\varphi \rightarrow \Delta E \rightarrow \Delta N\}$ is responsible for the null and hence the splitting. By considering the numerator and denominator dynamics of the above path, we obtained the following approximate expressions for the low-side-band (LSB) peak $(f_{\mathrm{LSB}})$ [27] and the null $(f_N)$ frequency positions in the IM response of the laser:

$$f_v = \frac{c}{L_e}\left(m - C_v\frac{B_v}{A_v}\frac{1}{\left(1+\sqrt{1-3\dfrac{A_v}{B_v^2}}\right)}\right) \qquad v \in \{\mathrm{LSB,\ Null}\} \tag{18a}$$

with

$$A_v = 2m\pi + \chi_v^2 \tag{18b}$$

$$B_v = 2m\pi\chi_v + m^2\pi^2 \tag{18c}$$

$$\chi_v = 1 + \left(\frac{L_e}{n_e L}S_c\right)\delta_{\mathrm{LSB},v} + \left(\frac{L_e}{n_e L}(S_c + \alpha C_c\sqrt{1+2\epsilon I_S})\right)\delta_{N,v} \tag{18d}$$

$$C_v = \left(\frac{3}{\pi^2}\right)\delta_{\mathrm{LSB},v} + \left(\frac{3}{10\pi}\right)\delta_{N,v} \tag{18e}$$

where $m$ $(m \leq 6)$ is the harmonic number of the external cavity resonance peak, and $\delta_{i,v}$ is the Kronecker Delta function. Expressions for $C_C$ and $S_C$ are given in Appendix D. The other parameters are given in Table I. Fig. 12 shows the analytical and simulated results for null frequency versus bias current, while similar results for the LSB peak are given in Fig. 13. Good agreement between simulated and analytical results were observed in both cases. Equations (18a)–(18e) also provide an qualitative picture of the dependence of splitting on $\alpha, R_2, \epsilon$, and $L_e$.

### *B. IMD Spectra*

In this section, we show that, IMD spectra relative to carrier C (i.e., *IMD/C*) exhibit complex splitting characteristics under direct small-signal modulation. The criteria used to calculate *IMD/C* is similar to the definition by Nagarajan *et al.* [29] which was described in Section II-C in the context of a

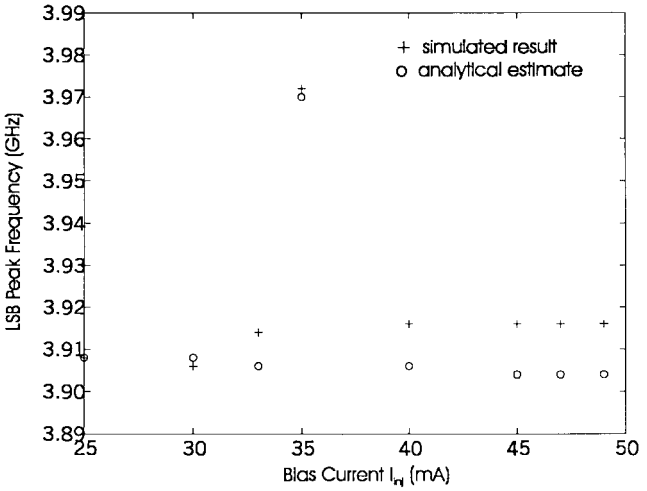


Fig. 12. Null position in resonance-peak splitting of IM response (at fundamental resonance harmonic). This figure shows the accuracy of the (14a)–(14e) with simulated results.

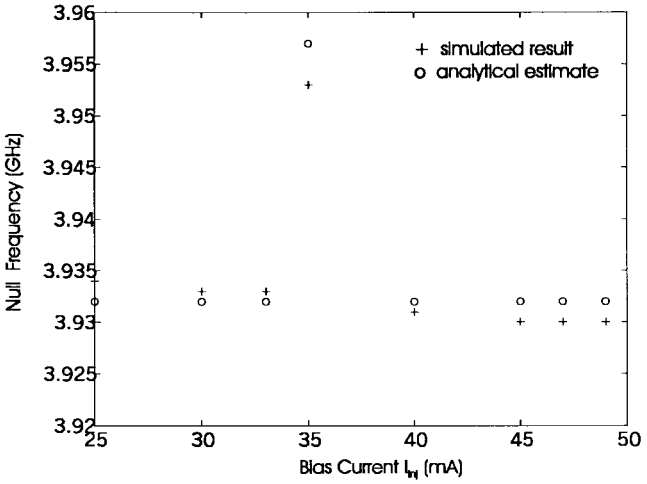


Fig. 13. LSB peak position in resonance-peak splitting of IM response (at fundamental resonance harmonic). This figure shows the accuracy of (14a)–(14e) with simulated results.

Volterra function formalism. Fig. 14 shows the IMD response for a 4-GHz FGEC laser, for the data given in Table I. It shows the appearance of splitting close to 4 GHz, and a trend for the enhancement of low frequency pseudopeaks as the frequency increases to the second cavity resonance harmonic (i.e., 8 GHz). It also shows the subsidiary peaks spaced between the cavity resonances. These subsidiary peaks have no importance to practical resonance transmission schemes because they are limited to narrow-band transmission around cavity resonance peaks. Nagarajan *et al.* [29] have explained the appearance of the subsidiary peaks in greater detail. Fig. 14 also shows an enlarged view of IMD response close to 4 GHz. It shows that RPSS appears as double nulls for the fundamental resonance. At higher frequencies, it is clear that the lower frequency peaks around the fundamental resonance are enhanced, while the high frequency peak is suppressed (see enlarged view around 8 GHz). This same trend was previously observed in the IM and RIN spectra (see Figs. 5 and 6). Fig. 14 also shows that as the harmonic number increases, the spectral splitting

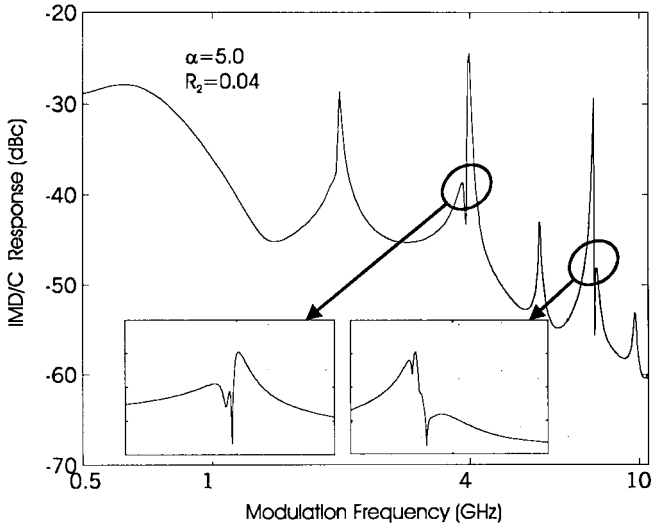


Fig. 14. IMD/C response of FGEC laser with 4-GHz external cavity at 40.0-mA bias current.

in subsidiary peaks tends to decrease. Similar trends were previously demonstrated for IM and RIN spectra.

## IV. Conclusion

A detailed model for fiber grating external cavity semiconductor lasers has been developed. Leakage current and parasitic effects are included in this model. To the best of our knowledge, this model represents the first unified study of semiconductor lasers subject to strong feedback for steady-state and periodically modulated (small-signal) conditions which includes noise and distortion effects. The composite system, consisting of external fiber grating cavity, solitary laser diode, chip and package parasitics, and leakage current induced nonlinearity was solved analytically in the small-signal regime using a Volterra functional series expansion method. We used this model to analyze the appearance of narrow peaks close to the harmonics of the cavity resonance frequency in the noise and modulated spectra. We showed that experimentally observed characteristics such as a variation of null position with dc-bias current. Our simulations showed that the form of the modulation spectrum is dependent on which harmonic is being used. Detailed simulations of IMD showed that IMD spectra experience more complex splitting patterns than the IM and RIN spectra. However as with the IM and RIN spectra, these complex splitting characteristics in IMD spectra reduce around higher harmonics. A detailed explanation using signal flow graphs was given showing that the appearance of narrow peaks and nulls close to the external cavity resonance harmonics in the noise and modulation spectra results from complex amplitude-phase coupling between active and passive resonant cavities. We identified that both the linewidth enhancement factor and residual facet reflectivity need to be minimized in order to reduce these spectral splitting phenomena, and have presented analytical formulae to quantify their effect.

## Appendix A

In this appendix, we outline the procedure for obtaining Volterra kernels for composite, intrinsic laser rate equations.

*1. Perturbation Expansion Coefficients*

$$\frac{\wp(1]}{\wp\langle 1\rangle} = \Bigg(-\Gamma\epsilon a V_g H(\omega_S)(N_S - N_t) I_S \Big/ (1+2\epsilon I_S)^{3/2} + \mathrm{Im}\bigg(\frac{d\ln(f(\omega_S))}{d\omega_S \tau}\bigg)\Big/\tau_L\Bigg)$$

$$\frac{\wp(1]}{\wp\langle 2\rangle} = 2\,\mathrm{Re}\bigg(\frac{d\ln(f(\omega_S))}{d\omega_S\tau}\bigg)\Big/\tau_L$$

$$\frac{\wp(1]}{\wp\langle 3\rangle} = aV_g H(\omega_S) I_S/\sqrt{1+2\epsilon I_S}$$

$$\frac{\wp(2]}{\wp\langle 1\rangle} = -\mathrm{Re}\bigg(\frac{d\ln(f(\omega_S))}{d\omega_S\tau}\bigg)\Big/2\tau_L V I_S$$

$$\frac{\wp(2]}{\wp\langle 2\rangle} = \mathrm{Im}\bigg(\frac{d\ln(f(\omega_S))}{d\omega_S\tau}\bigg)\Big/\tau_L$$

$$\frac{\wp(2]}{\wp\langle 3\rangle} = \alpha_{\mathrm{gsp}} a V_g H(\omega_S)/2V$$

$$\frac{\wp(3]}{\wp\langle 3\rangle} = -(A + 2BN_S + 3CN_S^2) - aV_g I_S/\sqrt{1+2\epsilon I_S}$$

$$\frac{\wp(3]}{\wp\langle 1\rangle} = (\gamma\epsilon a V_g (N_S - N_t) I_S/(1+2\epsilon I_S)^{3/2} - \Gamma a V_g (N_S - N_t)/\sqrt{1+2\epsilon I_S})$$

$$\frac{\wp(1]}{\wp\langle\partial 2\rangle} = \Gamma a V_g \frac{dH(\omega_S)}{d\omega_S}(N - N_t) V I_S/\sqrt{1+2\epsilon I_S}$$

$$\frac{\wp(2]}{\wp\langle\partial 2\rangle} = \alpha_{\mathrm{gsp}}\Gamma a V_g \frac{dH(\omega_S)}{d\omega_s}(N_s - N_t)\Big/2$$

$$\frac{\wp(1]}{\wp\langle\diamondsuit_\tau 1\rangle} = -\mathrm{Im}\bigg(\frac{d\ln(f(\omega_S)}{d\omega_S\tau}\bigg)\Big/\tau_L$$

$$\frac{\wp(1]}{\wp\langle\diamondsuit_\tau 2\rangle} = -2\,\mathrm{Re}\bigg(\frac{d\ln(f(\omega_S)}{d\omega_S\tau}\bigg) V I_S\Big/\tau_L$$

$$\frac{\wp(2]}{\wp\langle\diamondsuit_\tau 1\rangle} = \mathrm{Re}\bigg(\frac{d\ln(f(\omega_S)}{d\omega_S\tau}\bigg)\Big/\tau_L V I_S$$

$$\frac{\wp(2]}{\wp\langle\diamondsuit_\tau 2\rangle} = -\mathrm{Im}\bigg(\frac{d\ln(f(\omega_S)}{d\omega_S\tau}\bigg)\Big/\tau_L$$

$$\frac{\wp(1]}{\wp\langle 11\rangle} = -\Gamma\epsilon a V_g H(\omega_S)(N_S - N_t)/V(1+2\epsilon I_S)^{3/2}$$

$$\frac{\wp(1]}{\wp\langle 12\rangle} = 2\,\mathrm{Re}\bigg(\frac{d\ln(f(\omega_S)}{d\omega_S\tau}\bigg)\Big/\tau_L$$

$$\frac{\wp(1]}{\wp\langle 13\rangle} = -\epsilon a V_g H(\omega_S)(N_S - N_t) I_S/V(1+2\epsilon I_S)^{3/2} + a V_g H(\omega_S)(N_S - N_t)/V\sqrt{(1+2\epsilon I_S)}$$

$$\frac{\wp(2]}{\wp\langle 11\rangle} = \mathrm{Re}\bigg(\frac{d\ln(f(\omega_S)}{d\omega_S\tau}\bigg)\Big/2\tau_L V^2 I_S^2$$

$$\frac{\wp(3]}{\wp\langle 11\rangle} = \Gamma\epsilon a V_g (N_S - N_t)/V(1+2\epsilon I_S)^{3/2}$$

$$\frac{\wp(3]}{\wp\langle 13\rangle} = \epsilon a V_g I_S/V(1+2\epsilon I_S)^{3/2} - aV_g/V\sqrt{(1+2\epsilon I_S)}$$

$$\frac{\wp(3]}{\wp\langle 33\rangle} = -(B + 3CN_S)/\Gamma V$$

$$\frac{\wp(1]}{\wp\langle 1\partial 2\rangle} = -\Gamma\epsilon a V_g \frac{dH(\omega_S)}{d\omega_S}(N_S - N_t) I_S\Big/(1+2\epsilon I_S)^{3/2} + \Gamma a V_g \frac{dH(\omega_S)}{d\omega_S}(N_S - N_t)\Big/\sqrt{(1+2\epsilon I_S)}$$

$$\frac{\wp(1]}{\wp\langle 3\partial 2\rangle} = a V_g \frac{dH(\omega_S)}{d\omega_S} I_S\Big/\sqrt{(1+2\epsilon I_S)}$$

$$\frac{\wp(2]}{\wp\langle 3\partial 2\rangle} = \alpha_{\mathrm{gsp}} a V_g \frac{dH(\omega_S)}{d\omega_S}\Big/2V$$

$$\frac{\wp(1]}{\wp\langle 1\diamondsuit_\tau 2\rangle} = -2\,\mathrm{Re}\bigg(\frac{d\ln(f(\omega_S)}{d\omega_S\tau}\bigg)\Big/\tau_L$$

$$\frac{\wp(2]}{\wp\langle 1\diamondsuit_\tau 1\rangle} = -\mathrm{Re}\bigg(\frac{d\ln(f(\omega_S)}{d\omega_S\tau}\bigg)\Big/2\tau_L V^2 I_S^2$$

$$\frac{\wp(1]}{\wp\langle 113\rangle} = -\epsilon\epsilon a V_g H(\omega_S)/V^2(1+2\epsilon I_S)^{3/2}$$

$$\frac{\wp(3]}{\wp\langle 113\rangle} = \epsilon\epsilon a V_g/V^2(1+2\epsilon I_S)^{3/2}$$

$$\frac{\wp(3]}{\wp\langle 333\rangle} = -\frac{C}{\Gamma^2 V^2}$$

$$\frac{\wp(1]}{\wp\langle 11\partial 2\rangle} = -\Gamma\epsilon a V_g \frac{dh(\omega_S)}{d\omega_S}(N_S - N_t)\Big/V(1+2\epsilon I_S)^{3/2}$$

$$\frac{\wp(1]}{\wp\langle 13\partial 2\rangle} = -\epsilon a V_g \frac{dH(\omega_S)}{d\omega_S} I_S\Big/V(1+2\epsilon I_S)^{3/2} + a V_g \frac{dH(\omega_S)}{d\omega_S}\Big/V\sqrt{(1+2\epsilon I_S)}.$$

*2. Volterra Kernels for Intrinsic, Composite Laser Model*

Assuming $N_1(\omega_1), N_2(\omega_1,\omega_2)$, and $N_3(\omega_1,\omega_2,\omega_3)$ represent the first-, second-, and third-order Volterra kernels for carrier density under modulation, we calculate the Volterra kernels, using perturbation expansion coefficients as follows:

$$\Im_\alpha \Xi_\alpha = \frac{1}{\alpha!}\Xi_\alpha, \qquad \alpha \in \{1,2,3\} \tag{A2.1}$$

where $\Xi_\alpha, \alpha \in \{1,2,3\}$ represent the first, second and third order Volterra kernels for the composite system as

$$\Xi_1 = [I_1(\omega), \varphi_1(\omega), N_1(\omega)]^T \tag{A2.2}$$

$$\Xi_2 = [I_2(\omega_1,\omega_2), \varphi_2(\omega_1,\omega_2), N_2(\omega_1,\omega_2)]^T \tag{A2.3}$$

$$\Xi_3 = [I_3(\omega_1,\omega_2,\omega_3), \varphi_3(\omega_1,\omega_2,\omega_3), N_3(\omega_1,\omega_2,\omega_3)]^T \tag{A2.4}$$

where $T$ denotes the matrix transpose operation. The linear-system identication matrices $\Im_\alpha, \alpha \in \{1,2,3\}$ can be written as follows:

If the frequency dependency of $\Im_1$ can be represented as $\Im_1, = \Im_1(\omega)$, then the higher linear, system identification matrices can be given as

$$\Im_2 = \Im_1(\omega_1+\omega_2) \quad \text{and} \quad \Im_3 = \Im_1(\omega_1+\omega_2+\omega_3),$$

where the coefficients of

$$\Im_1 \equiv \{\Im_{1\alpha\beta}\colon \alpha,\beta \in \{1,2,3\}\}$$

are given below:

$$\Im_{111} = -j\omega + \frac{\wp(1]}{\wp\langle 1\rangle} - \frac{\wp(1]}{\wp\lfloor\diamondsuit_\tau 1\rfloor}\exp(-j\omega\tau)$$

$$\Im_{112} = j\omega \frac{\wp(1]}{\wp[\partial 2]} + \frac{\wp(1]}{\wp[2]} + \frac{\wp(1]}{\wp[\Diamond_\tau 2]} \exp(-j\omega\tau)$$
$$\Im_{113} = \frac{\wp(1]}{\wp[3]} \quad \Im_{121} = \frac{\wp(2]}{\wp[1]} + \frac{\wp(2]}{\wp[\Diamond_\tau 1]} \exp(-j\omega\tau)$$
$$\Im_{122} = -j\omega + j\omega \frac{\wp(2]}{\wp[\partial 2]} + \frac{\wp(2]}{\wp[2]} + \frac{\wp(2]}{\wp[\Diamond_\tau 2]} \exp(-j\omega\tau)$$
$$\Im_{123} = \frac{\wp(2]}{\wp[3]} \quad \Im_{131} = \frac{\wp(3]}{\wp[1]};$$
$$\Im_{132} = 0; \quad \Im_{133} = -j\omega + \frac{(3]}{\wp[3]}.$$

The driving terms $\Xi_\alpha$: $\alpha \in \{1,2,3\}$, can be expressed using lower order Volterra kernels as follows:

$$-\Xi_1 = \left[0, 0, \frac{\wp(3]}{\wp[0]}\right]^T$$
$$-\Xi_{21} = \overset{(1,2)}{\underset{(\alpha,\beta)}{\curlywedge}} \left( \left( j\omega_\beta \frac{\wp(1]}{\wp[1\partial 2]} + \frac{\wp(1]}{\wp[12]} + \frac{\wp(1]}{\wp[1\Diamond_\tau 2]} \cdot \exp(-j\omega_\beta\tau) \right) I_1(\omega_\alpha)\varphi_1(\omega_\beta) \right) + \overset{(1,2)}{\underset{(\alpha,\beta)}{\curlywedge}} \left( j\omega_\beta \frac{\wp(1]}{\wp[3\partial 2]} N_1(\omega_\alpha)\varphi_1(\omega_\beta) + \frac{\wp(1]}{\wp[13]} \cdot N_1(\omega_\alpha)I_1(\omega_\beta) + \frac{\wp(1]}{\wp[11]} I_1(\omega_\alpha)I_1(\omega_\beta) \right)$$
$$-\Xi_{22} = \overset{(1,2)}{\underset{(\alpha,\beta)}{\curlywedge}} \left( j\omega_\beta \frac{\wp(2]}{\wp[1\partial 2]} N_1(\omega_\alpha)\varphi_1(\omega_\beta) + \left( \frac{\wp(2]}{\wp[11]} + \frac{\wp(2]}{\wp[1\Diamond_\tau 1]} \exp(-j\omega_\beta\tau) \right) \cdot I_1(\omega_\alpha)I_1(\omega_\beta) \right)$$
$$-\Xi_{23} = \overset{(1,2)}{\underset{(\alpha,\beta)}{\curlywedge}} \left( \frac{\wp(3]}{\wp[13]} I_1(\omega_\alpha)N_1(\omega_\beta) + \frac{\wp(3]}{\lfloor 11]} I_1(\omega_\alpha)I_1(\omega_\beta) + \frac{\wp(3]}{\wp[33]} N_1(\omega_\alpha)N_1(\omega_\beta) \right)$$
$$-\Xi_{31} = \overset{(1,2,3)}{\underset{(\alpha,\beta,\gamma)}{\curlywedge}} \left( \left( j(\omega_\alpha+\omega_\beta) \frac{\wp(1]}{\wp[1\partial 2]} + \frac{\wp(1]}{\wp[12]} + \frac{\wp(1]}{\wp[1\Diamond_\tau 2]} \exp(-j(\omega_\alpha+\omega_\beta)\tau) \right) \cdot \varphi_2(\omega_\alpha,\omega_\beta)I_1(\omega_\gamma) \right) + \overset{(1,2,3)}{\underset{(\alpha,\beta,\gamma)}{\curlywedge}} \left( \left( j\omega_\alpha \frac{\wp(1]}{\wp[1\partial 2]} + \frac{\wp(1]}{\wp[12]} + \frac{\wp(1]}{\wp[1\Diamond_\tau 2]} \exp(-j\omega_\alpha\tau) \right) \cdot \varphi_1(\omega_\alpha)I_2(\omega_\beta,\omega_\gamma) \right) + \overset{(1,2,3)}{\underset{(\alpha,\beta,\gamma)}{\curlywedge}} \left( \left( j(\omega_\alpha+\omega_\beta) \frac{\wp(1]}{\wp[3\partial 2]} \varphi_2(\omega_\alpha,\omega_\beta)N_1(\omega_\gamma) + j\omega_\alpha \frac{\wp(1]}{\wp[3\partial 2]} \varphi_1(\omega_\alpha)N_2(\omega_\beta,\omega_\gamma) \right) \right) + \overset{(1,2,3)}{\underset{(\alpha,\beta,\gamma)}{\curlywedge}} \left( \left( \frac{\wp(1]}{\wp[13]} I_2(\omega_\alpha,\omega_\beta)N_1(\omega_\gamma) + \frac{\wp(1]}{\wp[13]} \cdot N_2(\omega_\alpha,\omega_\beta)I_1(\omega_\gamma) + 2\frac{\wp(1]}{\wp[11]} \cdot I_1(\omega_\alpha)I_2(\omega_\alpha,\omega_\gamma) \right) \right) + \overset{(1,2,3)}{\underset{(\alpha,\beta,\gamma)}{\curlywedge}} \left( j\omega_\alpha \frac{\wp(1]}{\wp[13\partial 2]} \varphi_1(\omega_\alpha)(I_1(\omega_\beta)N_1(\omega_\gamma) + I_1(\omega_\gamma)N_1(\omega_\beta)) \right) + \overset{(1,2,3)}{\underset{(\alpha,\beta,\gamma)}{\curlywedge}} \left( 2\left( \frac{\wp(1]}{\wp[11\partial 2]} N_1(\omega_\gamma) + j\omega_\gamma\varphi_1(\omega_\tau) \right) \cdot I_1(\omega_\alpha)I_1(\omega_\beta) \right)$$
$$-\Xi_{32} = \overset{(1,2)}{\underset{(\alpha,\beta)}{\curlywedge}} \left( \left( 2\frac{\wp(2]}{\wp[11]} + \frac{\wp(2]}{\wp[1\Diamond_\tau 1]} (\exp(-j\omega_\alpha\tau) + \exp(-j(\omega_\beta+\omega_\gamma)\tau)) \right) \cdot I_1(\omega_\alpha)I_2(\omega_\beta,\omega_\gamma)_1 \right) + \overset{(1,2)}{\underset{(\alpha,\beta)}{\curlywedge}} \left( j\omega_\alpha \frac{\wp(2]}{\wp[23\partial 2]} \varphi_1(\omega_\alpha)N_2(\omega_\beta,\omega_\gamma) + j(\omega_\alpha+\omega_\beta)\frac{\wp(2]}{\wp[23\partial 2]} \varphi_2(\omega_\alpha,\omega_\beta)N_1(\omega_\gamma) \right)$$
$$-\Xi_{33} = \overset{(1,2)}{\underset{(\alpha,\beta)}{\curlywedge}} \left( 2\frac{\wp(3]}{\wp[11]} I_1(\omega_\alpha)I_2(\omega_\beta,\omega_\gamma) + 2\frac{\wp(3]}{\wp[33]} N_1(\omega_\alpha)N_2(\omega_\beta,\omega_\gamma)_1 \right) + \overset{(1,2)}{\underset{(\alpha,\beta)}{\curlywedge}} \left( 2\frac{\wp(3]}{\wp[113]} I_1(\omega_\alpha)I_1(\omega_\beta)N_1(\omega_\gamma) + 2\frac{\wp(3]}{\wp[333]} N_1(\omega_\alpha)N_1(\omega_\beta)N_1(\omega_\gamma) \right).$$

## APPENDIX B

In this appendix, we give calculated expressions for Volterra kernels of homo-junction laser model shown in Fig. 2. The variable definitions can be found in Table I. Defining the following auxiliary variables: $\gamma_0(\omega) = \sqrt[4]{1+\omega^2\tau_D^2}, \theta(\omega) = \tan^{-1}(\omega\tau_D)$ and calculating $v_0$ from the following implicit equation: $v_0 = \zeta \exp(v_L I_S - v_H I_{S0}(v_0 - 1))$; we use this quantity to define following frequency dependent quantities:

$$v_1(\omega) = v_0 \left( v_L I_S + v_H I_{S0}\gamma_0(\omega)(1-v_0) \cdot \exp\left(j\frac{\theta(\omega)}{2}\right) \right) \Big/ I_S(1 + v_H v_0 I_{S0})$$
$$v_2(\omega_1,\omega_2) = \overset{(\omega_1,\omega_2)}{\underset{(\alpha,\beta)}{\curlywedge}} \left( (v_1(\omega_\alpha)v_1(\omega_\beta)/2v_0^2) - \left( \gamma_0(\omega_\alpha)v_1(\omega_\beta)\exp\left(j\frac{\theta(\omega_\alpha)}{2}\right) \right) \cdot v_H I_{S0} \Big/ I_S \right) \Big/ \left( \frac{1}{v_0} + v_H I_{S0} \right)$$

where $v_L = qR_L/\eta kT, v_H = q(R_L+R_H)/\eta kT$. The value of $\zeta I_{S0}$ is given in Table I with $\zeta$ given as $\zeta = \exp(qV_S/\eta kT)$.

$$\gamma_{23}=\frac{G_C(\alpha(s+\epsilon G_F)+(\alpha C_S\sqrt{1+2\epsilon I_S}+C_C)(1-\exp(-s\tau))/\tau_1)}{(s(s+\epsilon G_F)+C_S(2s+\epsilon G_F)(1-\exp(-s\tau))/\tau_L+((C_S^2+C_C^2)/\tau_L^2)(1-\exp(-s\tau))^2)}$$

Using these expressions, we can write the following expressions for Volterra kernels in leakage model (see Fig. 2):

$$L_1(\omega)=1+\gamma_0(\omega)(1-v_0)\frac{I_{S0}}{I_S}\cdot\exp\left(j\frac{\theta(\omega)}{2}\right)-I_{S0}v_1(\omega) \tag{B1}$$

$$L_2(\omega_1,\omega_2)=-\sum_{(\alpha,\beta)}^{(\omega_1,\omega_2)}\left(\gamma_0(\omega_\alpha)v_1(\omega_\beta)\frac{I_{S0}}{I_S}\exp\left(j\frac{\theta(\omega_\alpha)}{2}\right)+I_{S0}v_2(\omega_\alpha,\omega_\beta)\right)\Big/2 \tag{B2}$$

$$L_2(\omega_1,\omega_2,\omega_3)=-\sum_{(\alpha,\beta,\gamma)}^{(\omega_1,\omega_2,\omega_3)}\left(\gamma_0(\omega_\alpha)v_2(\omega_\beta,\omega_\gamma)\frac{I_{S0}}{I_S}\cdot\exp\left(j\frac{\theta(\omega_\alpha)}{2}\right)\right)\Big/3. \tag{B3}$$

## Appendix C

In this appendix, we give detailed expressions of Volterra kernels for parasitic network: Variable definitions are given in Table I (for details of model, see Fig. 2 )

$$P_1(\omega)=1/(j\omega C_P(R+R_LL_1(\omega))+(1+j\omega C_P(R_P+j\omega L_P))\cdot(1+j\omega C_S(R_S+R_LL_1(\omega)))) \tag{C1}$$

$$P_2(\omega_1,\omega_2)=-j(\omega_1+\omega_2)(C_P+C_S\cdot(1+j(\omega_1+\omega_2)\cdot C_P(j(\omega_1+\omega_2)L_P+R_P)))\times R_LP_1(\omega_1)P_1(\omega_2)\cdot P_1(\omega_1+\omega_2)L_2(\omega_1,\omega_2)/2 \tag{C2}$$

$$P_3(\omega_1,\omega_2,\omega_3)=-j(\omega_1+\omega_2+\omega_3)\cdot(C_P+C_S(1+j\cdot(\omega_1+\omega_2+\omega_3)\cdot C_P(j(\omega_1+\omega_2+\omega_3)\cdot L_P+R_P)))\times R_LP_1(\omega_1+\omega_2+\omega_3)L_3(\omega_1,\omega_2,\omega_3)\cdot(2P_1(\omega_1)P_2(\omega_2,\omega_3)+P_1(\omega_1)P_1(\omega_2)P_1(\omega_3))/6. \tag{C3}$$

## Appendix D

This appendix gives the detailed expressions for branch gains of signal flow graphs in Fig. 11. Using the variables defined in Table I, and using (1)–(4), we define:

$$G_C=\Gamma aV_g/2\sqrt{1+2\epsilon I_S}$$
$$G_F=\Gamma aV_g(N_S-N_t)/2(1+2\epsilon I_S)^{3/2}$$
$$\tau_{N\text{eff}}=((A+2BN_S+3CN_S^2)^{-1}+(2G_CI_S/\Gamma)^{-1})^{-1}$$
$$C_C=-\mathrm{Re}\left(\frac{d\ln(f(\omega_S))}{d\omega_S\tau}\right)$$

and

$$C_S=-\mathrm{Im}\left(\frac{d\ln(f(\omega_S))}{d\omega_S\tau}\right).$$

Using the above expressions we can obtain the following expressions for the Laplace Transform of branch gains ($s$ is the transform domain variable):

$$\alpha_{30}=1/(s+1/\tau_{N\text{eff}}),\quad \alpha_{13}=G_C/(s+\epsilon G_F)$$
$$\alpha_{31}=-2G_FI_S(1+\epsilon I_S)/\Gamma(s+1/\tau_{N\text{eff}})$$
$$\alpha_{23}=\alpha G_C\sqrt{1+2\epsilon I_S}/s,\quad \beta_{30}=\alpha_{30},\quad \beta_{13}=\alpha_{13}$$
$$\beta_{31}=\alpha_{31},\quad \beta_{23}=\alpha_{23},\quad \beta_{22}=\beta_{11}$$
$$\beta_{11}=-C_S(1-\exp(-s\tau))/\tau_L(s+\epsilon G_F)$$
$$\beta_{21}=C_C(1-\exp(-s\tau))/\tau_Ls$$
$$\beta_{12}=-C_C(1-\exp(-s\tau))/\tau_L(s+\epsilon G_F)$$
$$\gamma_{30}=\alpha_{30},\quad \gamma_{31}=\alpha_{31}$$
$$\gamma_{13}=G_C/(s+\epsilon G_F+C_S(1-\exp(s\tau))/\tau_L)$$
$$\gamma_{32}=-C_C(1-\exp(-s\tau))/(s\tau_L+\epsilon G_F\tau_L+C_S(1-\exp(-s\tau)))$$

and the equation found at the top of the page.

## Acknowledgment

One of the authors, M. Premaratne, would like to thank Assoc. Prof. Y. B. Hua for encouragement and useful discussions and Grace Matthaei scholarship committee for financial assistance. The help given by Ms. J. Yates, Dr. J. Badcock, Mr. L. V. T. Nguyen, and Mr. T. Nirmalathas is also kindly appreciated.

## References

[1] R. Lang and K. Kobayashi, "External optical feedback effects on semiconductor injection laser properties," *IEEE J. Quantum Electron.*, vol. QE-16, pp. 347–355, Mar. 1980.

[2] A. Olsson and C. L. Tang, "Coherent optical interference effects in external cavity semiconductor lasers," *IEEE J. Quantum Electron.*, vol. QE-17, pp. 1320–1323, Aug. 1981.

[3] J. H. Osmundsen and N. Gade, "Influence of optical feedback on laser frequency spectrum and threshold conditions," *IEEE J. Quantum Electron.*, vol. QE-19, pp. 465–469, Mar. 1983.

[4] K. Kavano, T. Mukai, and O. Mitomi, "Optical output power fliuctuations due to reflected lightwaves in laser diode modules," *J. Lightwave Technol.*, vol. LT-4, pp. 1669–1667, Nov. 1986.

[5] W. Bludau, and R. Rossberg, "Characterization of laser-to-fiber coupling techniques by their optical feedback," *Appl. Opt.*, vol. 21, pp. 1933–1939, June 1982.

[6] P. Zorabedian, W. R. Trutna, and L. S. Cutler, "Bistability in grating-tuned external-cavity semiconductor lasers," *IEEE J. Quantum Electron.*, vol. QE-23, pp. 1855–1860, Nov. 1987.

[7] J. O. Binder, G. D. Cormack and A. Somani, "Intermodal tuning characteristics of an InGaAsP laser with optical feedback from an external grating reflector," *IEEE J. Quantum Electron.*, vol. 26, pp. 1191–1198, July 1990.

[8] M. F. Ferreira, J. F. Rocha, and J. L. Pinto, "Noise and modulation performance of Fabry–Perot and DFB semiconductor lasers with arbitrary

external optical feedback," *Proc. Inst. Elect. Eng.*, vol. 137, pt. J., pp. 361–369, Dec. 1990.
[9] K. Vahala, J. Paslaski, and A. Yarive, "Observation of modulation speed enhancement, frequency modulation suppression, and phase noise reduction by detuned loading in a coupled cavity semiconductor laser," *Appl. Phys. Lett.*, vol. 46, pp. 1025–1027, June 1985.
[10] L. N. Langley, S. I. Turovets, and K. A. Shore, "Targeting in nonlinear dynamics of laser diodes," *Proc. Inst. Elect. Eng.*, vol. 142, pp. 157–161, June 1995.
[11] R. W. Tkach, and A. R. Chraplyvy, "Regimes of feedback effects in 1.5-$\mu$m distributed feedback lasers," *J. Lightwave Technol.*, vol. LT-4, pp. 1655–1661, Nov. 1986.
[12] P. Besnard, B. Meziane, and G. M. Stephan, "Feedback phenomena in a semiconductor laser induced by distant reflectors," *IEEE J. Quantum Electorn.*, vol. 29, pp. 1271–1284, May 1993.
[13] R. Wyatt and W. J. Devlin, "10 kHz linewidth 1.5 $\mu$m InGaAsP External cavity laser with 55 nm tuning range," *Electron. Lett.*, vol. 19, pp. 110–112, Jan. 1983.
[14] R. F. Kazarinov, C. H. Henry, and N. A. Olsson, "Narrow-band resonant optical reflectors and resonant optical transformers for laser stabilization and wavelength division multiplexing," *IEEE J. Quantum Electron.*, vol. QE-23, pp. 1419–1425, Sept. 1987.
[15] N. A. Olsson, C. H. Henry, R. F. Kazarinov, H. J. Lee, and K. J. Orlowsky, "Performance characteristics of a 1.5 $\mu$m single frequency semiconductor laser with an external waveguide Bragg reflector," *IEEE J. Quantum Electron.*, vol. 24, pp. 143–147, Feb. 1988.
[16] C. T. Sullivan, W. S. C. Chang, and R.-X. Lu, "External Bragg-reflector lasers," in *Proc. Tenth Anniv. National Science Foundation Grantee-User Meet. Optical Communication Systems*, J. R. Whiney, Ed., Univ. of California Berkeley, 1982, pp. 28–32.
[17] J. M. Hammer, C. C. Neil, N. W. Carlson, M. T. Duffy, and J. M. Shaw, "Single-wavelength operation of the hybrid-external Bragg-reflector-waveguide laser under dynamic conditions," *Appl. Phys. Lett.*, vol. 47., pp. 183–185, Aug. 1985.
[18] N. A. Olsson, C. H. Henry, R. F. Kazarinov, H. J. Lee, and B. H. Johnson, "Relation between chirp and linewidth reduction in external Bragg reflector semiconductor lasers," *Appl. Phys. Lett.*, vol. 47, pp. 183–185, Aug. 1985.
[19] P. A. Morton, V. Mizrahi, P. A. Andrekson, T. Tanbun-Ek, R. A. Logan, D. L. Coblentz, A. M. Sergent, and K. W. Wecht, "Hybrid soliton pulse source with fiber external cavity and Bragg reflector," *Electron. Lett.*, vol. 28, pp. 561–562, 1992.
[20] A. S. Daryoush, "Optical synchronization of millimeter-wave oscillators for distributed artuctures." *IEEE Trans. Microwave Theory Tech.*, vol. 38, pp. 467–476, 1990.
[21] S. Levy, R. Nagarajan, A. Mar, P. Humphrey, and J. E. Bowers, "Fiber-optic PSK subcarrier transmission at 35 GHz using a resonantly enhanced semiconductor laser," *Electron. Lett.*, vol. 28, pp. 2103–2104, Oct. 1992.
[22] S. Levy, R. Nagarajan, R. J. Helkey, P. Humphrey, and J. E. Bowers, "Millimeter wave fiber-optic PSK subcarrier transmission at 35 GHz over 6.3 km using a grating external cavity semiconductor laser," *Electorn. Lett.*, vol. 29, pp. 690–691, Apr. 1993.
[23] R. Nagarajan, S. Levy, A. Mar, and J. E. Bowers, "Resonantly enhanced semiconductor lasers for efficient transmission of millimeter wave modulated light," *IEEE Phtonic Technol. Lett.*, vol. 5, pp. 4–6, Jan. 1993.
[24] S. Levy, R. Nagarajan, A. Mar, P. Humphrey, and J. E. Bowers, "Fiber-optic PSK subcarrier transmission at 35 GHz using a resonantly enhanced semiconductor laser," *Electron. Lett.*, vol. 28, pp. 2103–2104, Oct. 1992.
[25] S. Levy, R. Nagarajan, R. J. Helkey, P. Humphrey, and J. E. Bowers, "Millimeter wave fiber-optic PSK subcarrier transmission at 35 GHz over 6.3 km using a grating external cavity semiconductor laser," *Electorn. Lett.*, vol. 29, pp. 690–691, Apr. 1993.
[26] R. Nagarajan, S. Levy, A. Mar, and J. E. Bowers, "Resonantly enhanced semiconductor lasers for efficient transmission of millimeter wave modulated light," *IEEE Photon. Technol. Lett.*, vol. 5, pp. 4–6, Jan. 1993.
[27] Z. Ahmed and R. S. Tucker, "Small-signal IM response of grating-terminated external cavity semiconductor lasers," *IEEE J. Select. Topics Quantum Electron.*, vol. 1, pp. 505–515, June 1995.
[28] L. A. Glasser, "A linearized theory for the diode laser in an external cavity," *IEEE J. Quantum Electron.*, vol. QE-16, pp. 525–531, 1980.
[29] R. Nagarajan, S. Levy, and J. E. Bowers, "Millimeter wave narrow-band optical fiber links using external cavity semiconductor lasers," *J. Lightwave Technol.*, vol. 12, pp. 127–136, Jan. 1994.
[30] M. S. Lin, S. J. Wang, and N. K. Dutta, "Measurements and modeling of the harmonic distortion in InGaAsP distributed feedback lasers," *IEEE J. Quantum Electron.*, vol. 26, pp. 998–1004, June 1990.
[31] L. Hassine, Z. Toffino, F. L. Lagarrigue, A. Destrez, and C. Birocheau, "Volterra functional series expansion for semiconductor lasers under modulation," *IEEE J. Quantum Electron.*, vol. 30, pp. 918–928, Apr. 1994.
[32] J. D. Park, D. S. Seo, and J. G. McInerney, "Self-pulsations in strongly coupled asymmetric external cavity semiconductor lasers," *IEEE J. Quantum Electron.*, vol. 26, pp. 1353–1362, Aug. 1990.
[33] H. Rong-Qing and T. Shang-Ping, "Improved rate equations for external cavity semiconductor lasers," *IEEE J. Quantum Electron.*, vol. 25, pp. 1580–1584, June 1989.
[34] P. A. Morton, V. Mizrahi, T. Tanun-Ek, R. A. Logan, P. J. Lemaire, H. M. Presby, T. Erdogan, S. L. Woodward, J. E. Sipe, M. R. Phillips, A. M. Sergent and K. W. Wecht, "Stable single mode hybrid laser with high power and narrow linewidth," *Appl. Phys. Lett.*, vol. 64, pp. 2634–2636, May 1994.
[35] C. R. Doerr, M. Zirngibl, and C. H. Joyner, "Single longitudinal mode stability via wave mixing in long-cavity semiconductor lasers," *IEEE Photon. Technol. Lett.*, vol. 7, no. 9, Sept. 1995.
[36] A. J. Lowery, "A qualitative comparison between two semiconductor laser amplifier equivalent circuit models," *IEEE J. Quantum Electron.*, vol. 26, pp. 1369–1375, Aug. 1990.
[37] M. Premaratne and A. J. Lowery, "Design of single-mode high-efficiency fiber grating external cavity lasers," in *21st Austral. Conf. Optical Fiber Technology (ACOFT-21 '96) Proc.*, Gold Coast, Queensland, Australia, Dec. 1996, pp. 171–174.
[38] G. P. Agrawal, "Effect of gain and index nonlinearities on single-mode dynamics in semiconductor lasers," *IEEE J. Quantum. Electron.*, vol. 26, pp. 1901–1909, Nov. 1990.
[39] ———, "Effect of nonlinear gain on intensity noise in single-mode semiconductor lasers," *Electron. Lett.*, vol. 27, pp. 232–233, Jan. 1991.
[40] H. Kogelnik and C. V. Shank, "Coupled-wave theory of distributed feedback lasers," *J. Appl. Phys.*, vol. 43, pp. 2327–2335, 1972.
[41] L. Poladian, "Variational technique for nonuniform gratings and distributed-feedback lasers," *J. Opt. Soc. Amer. A*, vol. 11, pp. 1846–1853, June 1994.
[42] P. Spano, S. Piazzolla, and Tamburrini, "Theory of noise in semiconductor lasers in the presence of optical feedback," *IEEE J. Quantum Electron.*, vol. QE-20, pp. 350–357, Apr. 1984.
[43] E. Bedrosian and S. O. Rice, "The output properties of Volterra systems (nonlinear systems with memory) driven by harmonic and gaussian inputs," *Proc. IEEE*, vol. 59, pp. 1688–1707, Dec. 1971.
[44] T. E. Darcie and R. S. Tucker, "Intermodulation and harmonic distortion in InGaAsP lasers," *Electron. Lett.*, vol. 21, pp. 665–666, Aug. 1985.
[45] R. S. Tucker, and I. P. Kaminow, "High-frequency characterization of directly modulated InGaAsP ridge waveguide and burried heterostructure lasers," *J. Lightwave Technol.*, vol. LT-2, pp. 385–393, Aug. 1984.
[46] S. Narayanan, "Transistor distortion analysis using Volterra series representation," *Bell Syst. Tech. J.*, pp. 991–1024, May 1967.
[47] H. Sato, T. Fujita, and K. Fujita, "Intensity fluctuations in semiconductor lasers coupled to external cavity," *IEEE J. Quantum Electron.*, vol. QE-21, pp. 46–50, 1985.
[48] M. Port and K. J. Ebeling, "Intensity noise dependence on the injection current of laser diode with optical feedback," *IEEE J. Quantum Electron.*, vol. 26, pp. 449–455, 1990.
[49] Z. Ahmed, "Dynamics of actively mode-locked semiconductor lasers," Ph.D. dessertation, Univ. of Melbourne, Australia, Aug. 1994.
[50] K. Ogita, *Modern Control Engineering*, 2nd ed. Englewood Cliffs, NJ: Prentice-Hall, 1990.

**Malin Premaratne** (S'95), photograph and biography not available at the time of publication.

**Arthur J. Lowery** (M'92–SM'96), for photograph and biography, see this issue, p. 289.

**Zaheer Ahmed** (S'92), for biography, see this issue, p. 269.

**Dalma Novak** (S'90–M'91), for photograph and biography, see this issue, p. 269.